JARS Journal of Applied Remote Sensing

RESEARCH PAPER

Advancement and demonstration of a perturbative retrieval technique for temperature profiling in the lower troposphere using differential absorption light detection and ranging

Owen Cruikshank,[a] **Luke Colberg**,[a] **Kevin S. Repasky**,[a,*] **Robert A. Stillwell**,[b] **and Scott M. Spuler**[b]

[a]Montana State University, Bozeman, Montana, United States
[b]NSF National Center for Atmospheric Research, Earth Observing Laboratory, Boulder, Colorado, United States

ABSTRACT. In response to a community-identified need for ground-based thermodynamic (TD) profiling of the troposphere, we present the further development and validation of a differential absorption LiDAR (DIAL) technique to retrieve temperature. This paper showcases the accuracy of temperature retrievals using a perturbative technique, combining a DIAL measurement of a temperature-sensitive oxygen (O_2) absorption profile with a high spectral resolution LiDAR measurement of the backscatter ratio profile near 770 nm. This study introduces three key advancements. First, the spectroscopic model used to represent the absorption of light by O_2 is enhanced via a more complete physical representation, improving measurement accuracy. Second, the error estimation and masking are developed using the bootstrapping technique. Third, we present a comparison of temperature profiles from our laboratory-based instrument with collocated radiosondes, evaluating the accuracy of our updated measurements. It is essential to clarify that the instrument described in this paper does not operate as a stand-alone TD profiler, as it is not capable of measuring water vapor (WV). Instead, we focus on demonstrating the perturbative retrieval technique with temperature profiles inferred using ancillary radiosonde WV profiles. Results from a full TD profiling instrument will be presented in a future publication. The laboratory-based LiDAR instrument was operated over a 6-month period between April 21, 2022, and September 22, 2022. During this time, we launched 40 radiosondes, providing reference data to validate the accuracy of the DIAL-based temperature profiles. The results indicate that DIAL-based temperature retrievals are within $\pm 2.5^{\circ}$C between 0.4 and 3 km (3.5 km) during daytime (nighttime) operation, using a 300-m range resolution and a 60-min time resolution.

Keywords: LiDAR; differential absorption LiDAR; aerosols; temperature; troposphere

Paper 240313G received May 21, 2024; revised Jul. 22, 2024; accepted Jul. 30, 2024; published Aug. 21, 2024.

1 Introduction

Thermodynamic (TD) profiling of the lower troposphere, including measurements of absolute humidity and temperature, can be used to partially define the state of the atmosphere. This TD profiling can provide important information for many atmospheric science and weather

*Address all correspondence to Kevin S. Repasky, repasky@montana.edu

forecasting applications and has been identified as vital by several reports.[1–5] As noted by Wulfmeyer et al.,[5] "networks of ground-based passive and active remote sensing systems operating in the optical, infrared (IR), and microwave (MW) spectral regions have the potential to close major gaps with respect to lower tropospheric TD profiling." As an example of the observation gaps, the National Research Council recommends approximately 400 next-generation weather stations across the continental United States.[1] These next-generation weather stations can include TD profiling LiDAR instruments that provide continuous profiling of the atmosphere and can be used to improve numerical weather forecasting by providing continuously updated information to constrain the numerical weather forecasting models. Initial work on the impacts from surface and profiler data for improving numerical weather forecasting is currently under study.[6] Wulfmeyer et al. recommended temperature profiling with a time resolution of $\leq$1 h and a vertical range resolution of 100 to 300 m in the convective mixed layer with a bias of $<$0.5 K and noise error $<$1 K[5] being needed for improved numerical weather forecasting. Atmospheric temperature profiling requirements for improving very short-range forecasting are defined by the World Meteorological Organization[7] as threshold (breakthrough): 2 to 3 K [1 K] accuracy for a time period of 60 min (10 to 30 min), vertical resolution of 1 to 2 km (0.3 to 0.5 km), and horizontal resolution of 50 to 200 km (10 to 20 km).

Of particular interest in this work is the temperature portion of the ground-based profiling. Ground-based temperature profiling of the lower troposphere has been accomplished using Raman LiDAR (e.g., Refs. 8–10) or passive remote sensing instruments, such as MW radiometers and IR spectrometers (e.g., Refs. 11–13). Passive remote sensing profilers typically have lower spatial and temporal resolution than active profilers; IR spectrometers have errors under cloudy conditions and have difficulty when temperature inversions are present. For Raman LiDARs, the small Raman scattering cross section, relative to elastic backscattering, requires high-power (class IV) lasers that can be complex. Raman LiDARs are unable to utilize etalons or ultra-narrow interference filters to block the solar background and thus provide reduced performance during the day. Furthermore, Raman LiDAR requires calibration.

As an alternative to these more established measurement techniques, differential absorption LiDAR (DIAL) is considered here. A diode-laser-based micropulse differential absorption LiDA (MPD) was developed as a low-cost network-deployable lower tropospheric profiler. The initial MPD instruments measured water vapor (WV) via the DIAL technique, but have expanded to provide full TD profiling through the addition of high spectral resolution LiDAR (HSRL) and O_2 DIAL channels.[14] Comparisons of the WV-only MPD instruments with passive and active ground-based instruments and field campaigns involving other observing systems have been discussed in previous work.[15,16]

The DIAL technique uses two closely spaced wavelengths: the online wavelength that is partially absorbed by the molecule of interest and the offline wavelength that is minimally absorbed by the molecule of interest. Because these wavelengths are very closely spaced, typically on the order of 0.1 nm, all other scattering and absorption effects are assumed to be the same. Thus, the only difference in the online and offline wavelengths after propagating through the atmosphere results from absorption by the molecule of interest, allowing the absorption coefficient to be measured directly. Common uses of DIAL have historically included number density profiling of WV, ozone, and other trace gases. If the number density of the molecule of interest is known, then the temperature profile can be inferred from the absorption coefficient profile when the absorption coefficient is temperature-sensitive. Theopold and Bösenberg demonstrated that atmospheric temperature measurements are theoretically possible using a temperature-sensitive oxygen (O_2) absorption line.[17] However, the temperature measurement is complicated in practice due to errors related to the Rayleigh–Brillouin broadening of the molecular backscatter signal. Bösenberg showed that, if the spectrum of the backscattered signal is not taken into account, errors of greater than 10°C can result.[18] Further practical issues arise from imperfect knowledge of the WV field. Theopold and Bösenberg[17] state that the temperature measurements require WV measurements because the number density of WV affects the estimated number density of O_2. The error associated is non-trivial based on pressure and relative humidity, but is generally higher with more WV.

Recently, a perturbative DIAL retrieval technique that accounts for the spectral shape of the scattered light has been developed;[19,20] it directly addresses the errors described by Bösenberg.

This technique uses an ancillary HSRL measurement of the aerosol backscatter ratio (BSR)—the ratio of the total backscatter to the molecular backscatter—to define the spectral shape of the backscattered signal and an ancillary DIAL measurement of WV. A perturbative solution that includes both a first-order and second-order correction is then used to obtain the absorption coefficient profile. Once the temperature-sensitive O_2 absorption profile is retrieved, an iterative technique is then used to obtain the temperature profile. Initial temperature profiling has been demonstrated using an MPD measurement of an O_2 absorption line at 769.7958 nm.[14]

In this paper, an experiment was conducted to further improve the efficacy of the DIAL method for temperature profiling. The laboratory-based instrument used for this study included a combined O_2 DIAL and potassium-based HSRL, but lacked the WV DIAL described in Spuler et al.[15] The instrument was operated continuously on the Montana State University (MSU) campus between April 21, 2022, and September 22, 2022. During this time, a total of 40 radiosondes were launched for comparison. The purpose of this paper is to describe improvements made to the temperature retrieval since Repasky et al.[19] and Stillwell et al.[14] and to perform an analysis of DIAL temperature retrieval profiles compared to temperature profiles measured using radiosondes. The improvements to the temperature retrieval include adding multiple absorption lines to the spectroscopic model, using an improved pressure model for the temperature retrieval, and applying a bootstrapping method that provides an estimate of error.

The retrieval described in this paper infers pressure assuming hydrostatic equilibrium from the temperature profile in an iterative fashion. Lapse rate estimates directly result from the range-resolved temperature retrieval. Combining the measured temperature and inferred pressure profiles, the potential temperature profile can be retrieved. Further combining the temperature profile with the WV absolute humidity profile allows for the retrieval of relative humidity and virtual potential temperature. With these basic TD quantities, atmospheric stability can be assessed. The purpose of this paper is to demonstrate the ability of the MPD to retrieve temperature profiles; we anticipate that future work will address the continued development of data products, such as relative humidity, potential temperature, and virtual potential temperature.

This paper is organized as follows. In Sec. 2, the theory for the DIAL-based temperature retrieval is discussed. Section 3 presents the data analysis process, including a brief discussion on a bootstrapping method for estimating the error in the retrieved temperature profile. A brief description of the instrument used in this study is presented in Sec. 4. Experimental results are presented in Sec. 5. A discussion of the experimental results is presented in Sec. 6. Finally, some brief concluding remarks are presented in Sec. 7.

2 Temperature Retrieval Theory

Theopold and Bösenberg[17] showed that a DIAL temperature retrieval is theoretically possible based on work performed in the prior decade.[21–24] They also showed that large errors, up to 10°C, occur if the lineshape of the backscattered signal is not considered. In the selected region of 770 nm, the Rayleigh–Brillouin broadened molecular backscatter has a linewidth of about 2 GHz, which is a similar spectral width to the selected O_2 absorption line, whereas the aerosol scattering linewidth is about equal to the laser linewidth (typically about 1 MHz). In short, light scattered by aerosols has nearly identical absorption on the propagation path from the LiDAR system to the scatterer as on the return trip. By contrast, light scattered by molecules has less absorption on the return trip to the LiDAR system than the outbound leg (assuming the laser is tuned to the absorption line center). Not accounting for this effect results in the measured absorption coefficient typically being lower than the absorption coefficient that would be expected assuming that laser light is not altered by scattering, where aerosol gradients accentuate the effect, and it is the cause of the large errors in DIAL temperature retrievals, as discussed by Bösenberg.[18]

2.1 O_2 Absorption Retrieval and Correction

To address this issue highlighted by Bösenberg,[18] the temperature retrieval used in this paper utilizes an HSRL to measure the BSR as well as a DIAL measurement of O_2 absorption. The first step involves a perturbative retrieval of a temperature-sensitive O_2 absorption coefficient that accounts for the lineshape of the scattered light. The second step uses an iterative retrieval

that incorporates the retrieved absorption profile to obtain the temperature profile. The reader is referred to Bunn et al.[20] and Repasky et al.[19] for complete details; the present work will focus on the differences and advancements beyond the methods presented in those two works.

The lineshape of the backscattered signal is

$$g_x(\nu, r) = \frac{1}{1 - \mathrm{BSR}(r)} h_x(\nu) + \frac{1}{\mathrm{BSR}(r)} [h_x(\nu) \otimes l(\nu, r)], \tag{1}$$

where $h_x(\nu)$ is the laser lineshape, $l(\nu, r)$ is the molecular backscatter broadened lineshape (represented here by a Rayleigh–Brillouin lineshape[25,26]), $\otimes$ is a symbol for the convolution operation, and the subscript x is either 1 for the online wavelength or 2 for the offline wavelength. For the work described in this paper, the laser lineshape, which is about three orders of magnitude narrower than the Rayleigh–Brillouin broadened lineshape, is assumed to be a delta function. The Rayleigh–Brillouin broadened lineshape is calculated following Binietoglou et al.[27] The variable r represents the range from the instrument, and ν represents the wavenumber. The BSR is defined as $\mathrm{BSR}(r) = \frac{\beta_a(r) + \beta_m(r)}{\beta_m(r)}$ and is measured directly by the HSRL. This is a major difference from early DIAL-based temperature profiling efforts, which leveraged Fernald/Klett-style inversions[18] for BSR. Here, $\beta_a(r)$ is the aerosol backscatter coefficient and $\beta_m(r)$ is the molecular backscatter coefficient.

A perturbative expansion to the LiDAR equation using knowledge of the BSR is used to retrieve the O_2 absorption coefficient, $\alpha_{O_2}(r)$. The O_2 absorption coefficient is written as an approximate sum of a zero-order term, $\alpha_{0\mathrm{th}}(r)$, and first and second-order corrections, $\Delta\alpha_{1\mathrm{st}}(r)$ and $\Delta\alpha_{2\mathrm{nd}}(r)$, respectively, so that

$$\alpha_{O_2}(r) \approx \alpha_{0\mathrm{th}}(r) + \Delta\alpha_{1\mathrm{st}}(r) + \Delta\alpha_{2\mathrm{nd}}(r). \tag{2}$$

The zero-order term, $\alpha_{0\mathrm{th}}(r)$, is found using the standard DIAL equation, which is written as

$$\alpha_{0\mathrm{th}}(r) = \alpha_2(r) - \frac{1}{2\Delta r} \ln\left(\frac{N_1(r + \Delta r) N_2(r)}{N_1(r) N_2(r + \Delta r)}\right). \tag{3}$$

In this case, the offline absorption, $\alpha_2(r)$, is three orders of magnitude smaller than the online absorption and is estimated using a modeled atmosphere. The received signal at range r is represented by N, and Δr is the LiDAR range bin. The first and second-order correction terms incorporate the BSR and account for the Rayleigh–Brillouin broadening of the molecularly scattered signal. The first and second-order terms are unchanged from Bunn et al.[20] and Repasky et al.[19] and are omitted here for brevity.

2.2 Iterative Temperature Retrieval

With the measured absorption coefficient, α_{O_2}, that is corrected for Rayleigh–Brillouin effects, the retrieval uses an iterative process to determine temperature from an O_2 absorption profile. This process is described in detail in Repasky et al.[19] for a single absorption line and is expanded here to include multiple absorption lines. This is necessary because there are a number of extra confounding lines in the oxygen A-band that occur near the absorption line of interest. These lines have different temperature sensitivities and overall line strengths that result from different vibrational ground states, isotopes of diatomic oxygen, and electric quadrupole transitions. Figure 1 shows the O_2 absorption using all cabsorption lines in the region of interest obtained from the high-resolution transmission molecular absorption database (HITRAN) database.[28–30] Panel (a) shows the absorption at sea-level and at 4 km above mean sea-level using the United States (US) standard atmosphere. The online and offline wavelengths are shown as vertical dashed lines. The absorption line strength decreases with height due to a lower temperature at 4 km. Likewise, lines narrow with height due to the lower pressure. Panel (b) shows individual absorption lines and the total absorption. The main absorption line is from the Ref. 16: O_2, $v'' = 0$ band around 769.8 nm. There is one confounding line that contributes significantly and is shown in Fig. 1 from the Ref. 16: O_2, $v'' = 1$ band also near 769.8 nm.

The iterative temperature retrieval starts with an initial temperature guess, $T_i(r)$, and then uses the retrieved O_2 absorption profile to calculate a correction to the temperature profile, $\Delta T(r)$. This temperature correction is used to update the temperature profile, as shown in

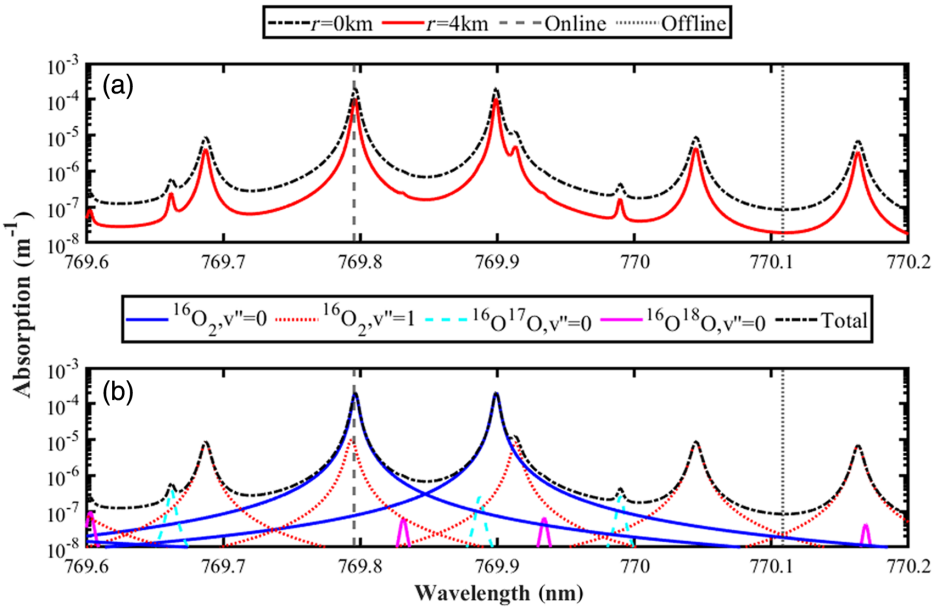

Fig. 1 (a) O_2 absorption spectrum in the wavelength region of interest. The model is shown at sea-level and at a range of 4 km above mean sea-level (assuming the 1976 US Standard Atmosphere). (b) The total O_2 absorption spectrum as the bold blue line and each individual absorption line in the region of interest at the surface. Dashed vertical lines represent the online and offline DIAL wavelengths. In this figure and throughout the text, all wavelengths are given as wavelengths in vacuum. This figure shows how the absorption changes with altitude and the many separate absorption lines contributing to total absorption.

Eq. (4), where i is the iteration number. The updated temperature profile is then used in the next iteration, along with the O_2 absorption profile, to calculate a new temperature correction. This process is repeated until the temperature profile converges, i.e., changes in temperature are small on the order of 0.01°C, typically within 20 iterations. The temperature correction is given as

$$T_{i+1}(r) = T_i(r) + \Delta T(r) = T_i(r)\left[1 + \frac{\Delta T(r)}{T_i(r)}\right]. \tag{4}$$

The total O_2 absorption is the sum of each individual absorption line, given as

$$\alpha_{O_2}(\nu, r) = \sum_k a_k(\nu, r), \tag{5}$$

where k represents the absorption lines of interest. The absorption for each line k is calculated as[31]

$$\alpha_k(\nu, r) = \frac{S_{0k}(T_0)T_0 P(r)\exp\left(\frac{\varepsilon_k}{k_B T_0}\right)}{k_B} g_k(\nu - \nu_0, r)q(r)T(r)^{-2}\exp\left(\frac{-\varepsilon_k}{k_B T(r)}\right), \tag{6}$$

where S_0 is the absorption line strength, T_0 is the HITRAN reference temperature, T is the temperature, P is the pressure, ε is the ground state energy, k_B is the Boltzmann constant, g is the Voigt absorption lineshape, and q is the O_2 atmospheric mixing ratio. The pressure as a function of altitude is updated along with the temperature using

$$P(r) = P_s \exp\left(\int_0^r \frac{g_0 m_{\text{air}}}{k_B T(r')} dr'\right), \tag{7}$$

where P_s is the surface pressure, g_0 is the gravitational acceleration, and m_{air} is the molecular mass of air. The equation for pressure, Eq. (7), is substituted into Eq. (6). The ΔT in the current iteration is found using the expansion from Eq. (4), where $\frac{\Delta T(r)}{T_i(r)} \ll 1$ and keeping first-order terms containing $T(r)$ in Eq. (6) to find

$$\Delta T = \frac{\alpha_{O_2}(r) - \sum_{k=1}^{\text{No. of lines}} C_{1k}(r) C_{2k}(r) g_k(\nu - \nu_0, r) q(r)}{\sum_{k=1}^{\text{No. of lines}} C_{1k}(r) C_{2k}(r) C_{3k} g_k(\nu - \nu_0, r) q(r)}, \tag{8}$$

where

$$C_{1,k} = \frac{S_{0k}(T_0) T_0 P_s \exp\left(\frac{\epsilon_k}{k_B T_0}\right)}{k_B}, \tag{9}$$

$$C_{2,k}(r) = T_i(r)^{-2} \exp\left(\frac{-\epsilon_k}{k_B T_i(r)}\right) \exp\left(\frac{-g_0 m_{\text{air}}}{k_B} \int_0^r \frac{1}{T_i(r')} \mathrm{d}r'\right), \tag{10}$$

and

$$C_{3,k}(r) = \frac{-2}{T_i(r)} + \frac{\epsilon_k}{k_B T_i^2(r)} + \frac{g_0 m_{\text{air}}}{k_B} \int_0^r \frac{1}{T_i^2(r')} \mathrm{d}r'. \tag{11}$$

The subscripts k represent the separate absorption lines, and the subscripts i represent the temperature retrieval iteration. Note that Eqs. (8)–(11) can be compared to Repasky et al.[19] Eqs. (25) and (26a–c), respectively. The prime difference is the addition of multiple lines and the different barometric formula used for pressure. Here, we do not assume a single value for the lapse rate but rather leave the temperature profile within the integral term.

3 Data Analysis Algorithm

The temperature retrieval and error analysis are written in MATLAB. Section 3.1 describes the steps of the temperature retrieval from data to HSRL retrieval, absorption retrieval, and finally temperature. Section 3.2 describes the bootstrapping method of error estimation.

3.1 Temperature Retrieval Program

The temperature retrieval program processes raw photon data (plus surface T and P) and retrieves temperature profiles with an estimate of error. The return photon signals for both the online and offline wavelengths for both the molecular and total receiver channels, including integration in time and range, are first loaded and pre-processed and then prepared for error analysis (discussed in Sec. 3.2). The HSRL retrieval is discussed in detail in Hayman and Spuler[32] and Stillwell et al.[14] and used here without modification with measured calibration data files specific to this instrument.

In the next step of the temperature retrieval algorithm, the perturbative retrieval is applied to find the O_2 absorption coefficient. For this retrieval, the online and offline wavelength data from the total channel are used. This process is described in detail in Sec. 3.2. First, the spectrum of the backscattered light is estimated using the BSR retrieved from the HSRL with a Rayleigh–Brillouin lineshape applied to the molecularly scattered light. The Rayleigh–Brillouin lineshape is weakly temperature-dependent, so an approximation is made. We assume a simple starting temperature profile that is based on the surface temperature and lapse rate of 6.5°C/km. However, because the model temperature profile is updated each iteration, the choice of the starting lapse rate does not affect the final temperature profile (except possibly slowing the final solution convergence given a starting guess that is nearer/further from the final solution). It should be noted that the Rayleigh–Brillouin lineshape changes from an full width at half maximum (FWHM) = 2.18 GHz at 27°C to an FWHM = 2.16 GHz at 17°C, i.e., HSRL measurements are not exceptionally sensitive to temperature. Furthermore, the Rayleigh–Brillouin lineshape comes into the perturbative retrieval through the first and second-order correction terms, which affect the overall absorption coefficient by ~10% and 1%, respectively. Thus, errors in the assumed initial temperature profile used to determine the lineshape for the molecularly scattered light will affect the retrieved absorption coefficient minimally. Next, the absorption linewidth is calculated using the HITRAN parameters and a Voigt profile. The Rayleigh-–Brillouin lineshape and the absorption lineshape are calculated using principal component analysis.[33] The zero-order, first-order, and second-order corrections are then calculated and used to retrieve the total O_2 absorption profile.

The next step in the retrieval algorithm is to use the retrieved O_2 absorption profile to complete the iterative temperature retrieval. First, an initial temperature profile (T_i) is modeled using the surface temperature and lapse rate. Next, a pressure profile is calculated as described in Sec. 2. The temperature deviation ΔT is then calculated using the retrieved absorption coefficient and Eq. (8). A new temperature profile (T_{i+i}) is then calculated by adding the initial temperature guess (T_i) and ΔT. This new temperature profile is then used as the temperature guess and pressure on the next iteration of the temperature retrieval. This process is repeated using the updated temperature and pressure profiles until the temperature profile converges (i.e., when ΔT goes to within some tolerance of zero). The iterative temperature retrieval converges in ~20 iterations.

3.2 Error Analysis

Standard LiDAR analysis has heavily leveraged the linear propagation of error, i.e., taking a Taylor expansion of the equation of interest and assuming Poisson statistics to bound measurement uncertainty. This common method fails in this case for a number of reasons. An estimate of the error is difficult for the two-step temperature retrieval described above due to the nonlinear nature of the retrieval. Furthermore, the errors observed are not all Poisson distributed, including uncertainties in BSR and WV profiles. In lieu of standard error propagation techniques, a bootstrapping method for estimating the error is used. This method has been developed for the WV MPD[15] and adapted for temperature profiling.

The bootstrapping method can be used to estimate multiple sources of error, such as the shot noise of the detectors, initial conditions of temperature and pressure, error in wavelength stability, and in HSRL calibration measurements. However, bootstrapping shows only variability in error and cannot show consistent bias in error. The dominant source of error is due to the shot noise in the detectors because of a low signal-to-noise ratio; therefore, this paper only considers shot noise in the bootstrapping error estimate.

The O_2 online combined, O_2 offline combined, O_2 online molecular, and O_2 offline molecular (and WV online and offline for other MPD instruments) photon number profiles are summed by the MPD instrument over 2 s and then written to the data file. The bootstrapping error estimate starts with a Poisson thinning technique in which these profiles are randomly split into two statistically independent but identically distributed number profiles for both the online and offline wavelengths.[34] This splitting is accomplished by sampling a binomial distribution with a probability of 0.5 for each photon measurement. The two online and offline profiles are then processed using the temperature retrieval (including the HSRL retrieval and absorption retrieval), yielding two unique temperature profiles: $T^f(r)$ and $T^g(r)$. The Poisson thinning and temperature processing is repeated until the variance estimate converges. This process tends to converge in ~20 iterations, and the standard deviation of the multiple temperature profiles is then used as an error estimate:[15]

$$\sigma_T^2(r) \approx \frac{1}{2[B-1]} \sum_{b=1}^{B} [T^{b,f}(r) - T^{b,g}(r)]^2, \tag{12}$$

where b is the iteration number; B is the total number of bootstrap iterations, which is defined to be > 1; and $\sigma_T(r)$ is the estimated error in °C.

4 Instrument Description

The instrument in this paper is a subset of the MPD architecture that has been developed by MSU and the National Center for Atmospheric Research (NCAR). The architecture was initially designed for WV profiling. A network of five full TD profiling MPDs has been constructed by NCAR for field use and includes the O_2-DIAL, HSRL, and WV DIAL in the same system using a common telescope. The interested reader can find the full details of the MPD architecture in Spuler et al.[14] The instrument in this paper is a laboratory demonstrator and does not include a WV DIAL needed for a full TD profiler.

The combined HSRL and O_2 DIAL were located in a roofport-equipped laboratory facility of MSU. Ancillary measurements of surface temperature and pressure were provided by a collocated weather station (Vaisala CS105, HMP45C) operated by the MSU Optical Remote Sensor Lab. The radiosonde station was located next to the roofport and allowed for the launching of

Vaisala RS92_KL radiosondes that are monitored using the Vaisala SPS220 with the GC25 ground check station. The DIAL-based temperature retrievals were compared to temperature profiles retrieved using the radiosondes.

5 Observational Data

The instrument described in Sec. 4 was operated between April 21, 2022, and September 22, 2022. Between April 21 and July 16, a pulse duration of 1 μs and a pulse repetition rate of 7 kHz were used. Between July 26 and September 22, a pulse duration of 750 ns and a pulse repetition rate of 8 kHz were used. The pulse length was changed in an attempt to address a consistent low-altitude bias, and the repetition rate was increased to account for the total pulse power loss. The bias is discussed in Sec. 6. A collocated radiosonde station was used to launch a total of 40 radiosondes over the course of the LiDAR operation, with 30 launched between April 21 and July 16 and the remaining 10 launched between July 26 and September 22. Radiosondes were launched at times to sample a variety of daytime and nighttime conditions. Some days have multiple radiosonde launches to track the evolution of the boundary layer for a separate study.

The retrieved temperature profile as a function of time and range is shown in Fig. 2, with a selected subsection in Fig. 3 to show more detail. Figures 2(a) and 2(c) show the retrieved temperature as a function of range and time for the April 21 to July 22 and July 26 to September 22 periods, respectively. Figures 2(b) and 2(d) show the corresponding surface temperature. The dashed black vertical lines indicate when radiosondes were launched. The WV mixing ratio used in the retrieval to calculate temperature for Figs. 2 and 3 was interpolated from radiosonde data. For the data presented in Figs. 2 and 3, a cloud mask and a signal-to-noise-ratio mask were applied. The cloud mask is a moving standard deviation window of the BSR with dimensions of 150 m and 20 min (two range bins and two time bins) and a threshold of 5 that is set to remove clouds. The temperature resolution is defined by a moving average with dimensions of 300 m in range and 60 min in time. Vertical resolution is limited by the need to reduce instrument noise. Other methods, such as the Poisson total variation method introduced by Hayman et al.,[35] significantly reduce noise for full TD retrievals but at the cost of computational expense. The signal-to-noise mask is created from the Poisson thinning process described in Sec. 3 with a threshold of 5°C. This combination of averaging and masking was chosen so the temperature mask covered up to 3.5 and 4 km in range and the temperature uncertainty from detector noise was within 5°C. Furthermore, data below 400 m are masked due to the relatively long pulse length of the MPD contaminating low-altitude bins.

Selected plots of the temperature as a function of range with comparisons to radiosondes are shown in Fig. 4. All radiosondes are shown for the interested reader in Sec. 8. The blue line is the temperature measured from the radiosonde, and the black line indicates the temperature retrieved using the LiDAR. The error bounds shown in red are estimated using the bootstrapping method. Figure 5 shows the same profiles but as a difference between DIAL profiles and radiosonde profiles. The profiles shown in Figs. 4 and 5 show good agreement with the radiosondes, including changes in temperature with altitude. During the summer months, surface air temperature is highly variable due to strong shortwave radiative heating. During the day, intense surface heating caused a super-adiabatic lapse rate, and during the night, radiative cooling caused temperature inversions at the surface. These effects are mostly confined below the first measurement bin of the temperature profile at 400 m. This can be seen in the radiosonde profiles between the ground level and 500 m in Fig. 4.

6 Discussion

This section discusses the LiDAR data presented in Sec. 5 and radiosonde data. The data presented are either from radiosondes (subscript radiosonde), absorption calculated from radiosonde measurements (subscript spectroscopic), or the DIAL instrument (subscript DIAL). Section 6.1 discusses the perturbative absorption correction from Sec. 2.1. Section 6.2 discusses the iterative temperature retrieval from Sec. 2.2. Section 6.3 discusses the DIAL temperature retrieval with radiosonde temperature measurements.

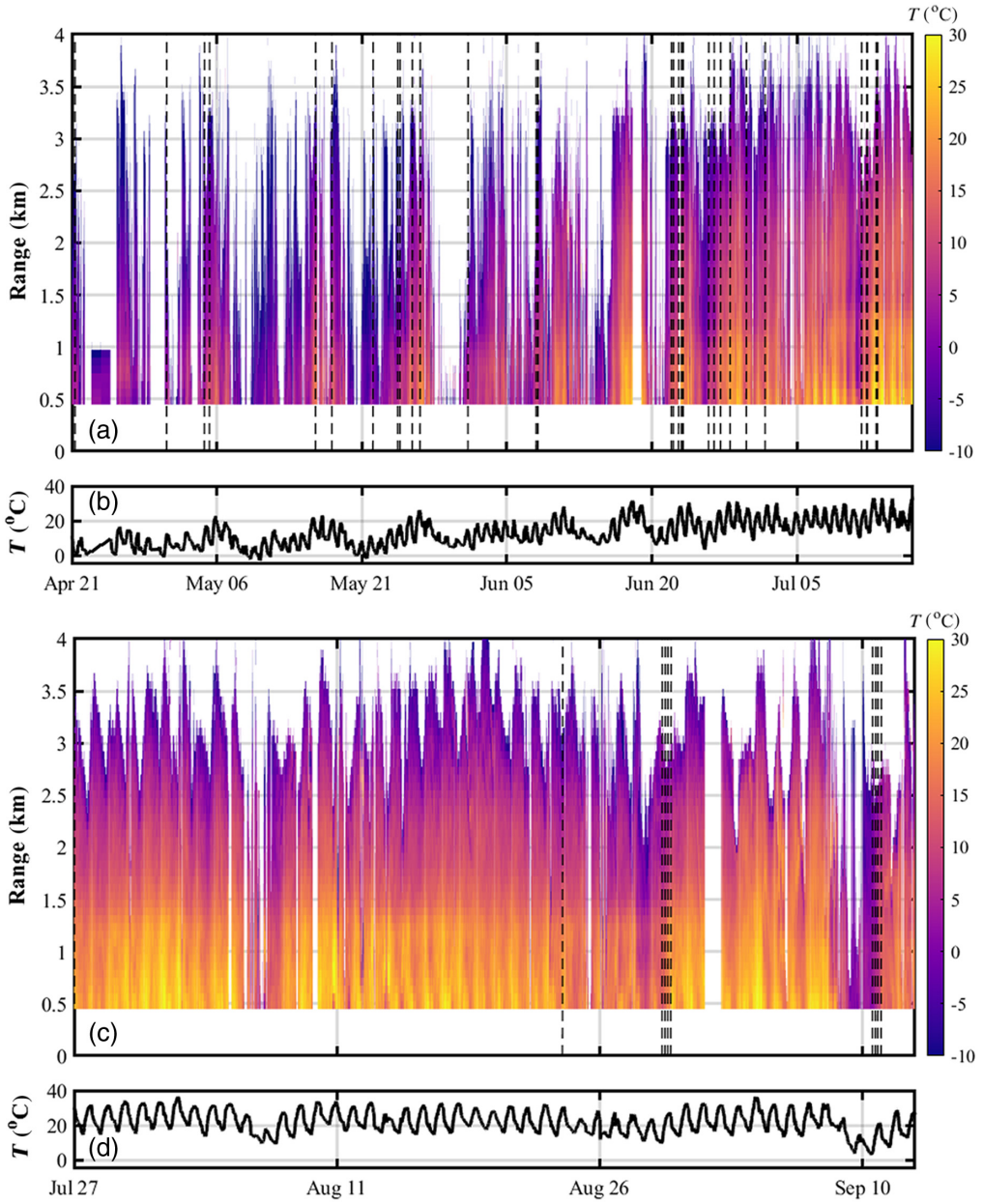

Fig. 2 (a)–(d) Temperature retrieval from the MSU O_2-DIAL and HSRL in the summer of 2022. Vertical dashed lines represent radiosonde launches. Areas in white represent a data mask. The data mask is from data availability, clouds, and a low signal-to-noise ratio. Time ticks are located at 00:00 UTC. This figure shows the LiDAR range and performance over many weeks of operation, including the diurnal cycle.

6.1 Perturbative Absorption Correction

The perturbative retrieval of the O_2 absorption coefficient utilizes the retrieved BSR to account for the broadened lineshape of the backscattered signal. A plot of the zero-order absorption, first-order correction, second-order correction, and total absorption are shown in Figs. 6(a)–6(d), respectively, for the same time period as Fig. 3. The BSR is shown in Fig. 6(e). For the O_2 absorption coefficient retrieval, the zero-order term tends to be too low due to the broadening of the molecularly scattered signal, i.e., observed absorption is less than what would be expected from pure aerosol scattering. Accordingly, the first-order correction term is mostly positive and is on the order of about 10% to the total absorption coefficient. The second-order correction term contributes about 1% to the total absorption coefficient. The first- and second-order correction

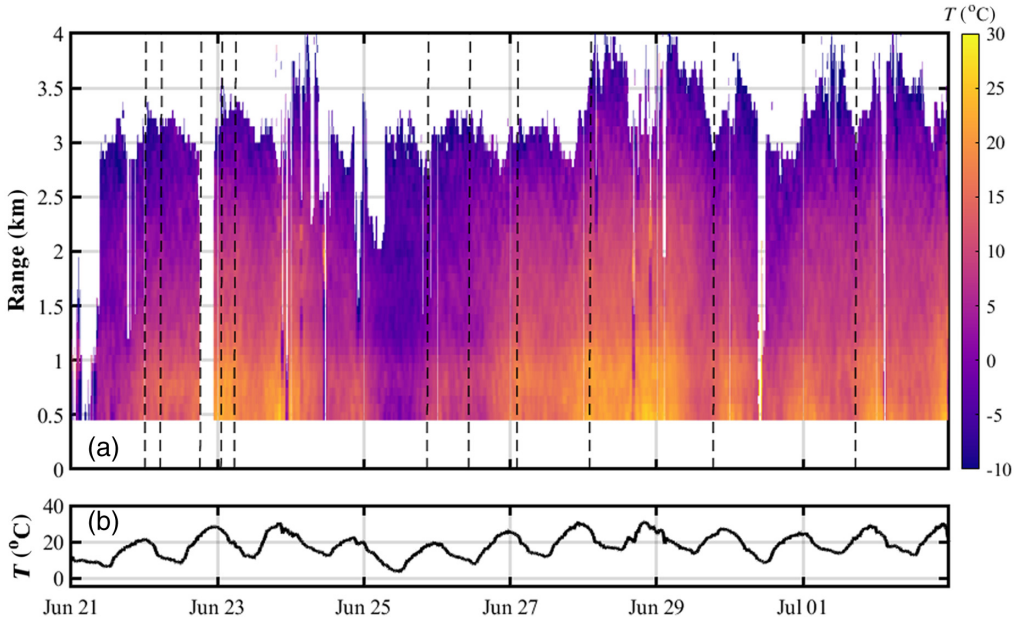

Fig. 3 (a) and (b) Selected section of the measurement period shown in Fig. 2. This selection was chosen to show finer detail than can be seen in Fig. 1. Time ticks are located at 00:00 UTC.

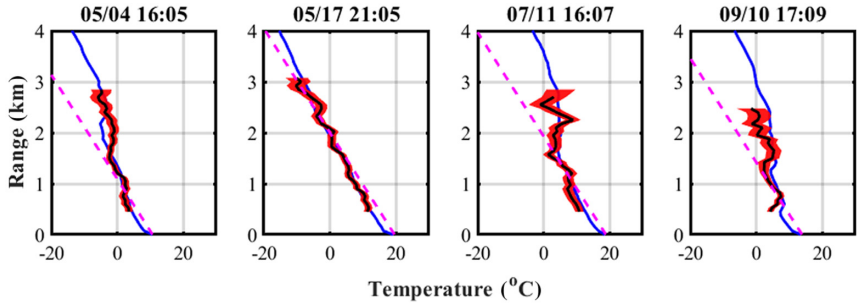

Fig. 4 Selected radiosonde profiles from the measurement period with the radiosonde temperature in blue, DIAL temperature in black, and error colored in light red shading. The dry adiabatic lapse rate (−9.8°C/km) is shown as the dashed line. The individual performance of the DIAL temperature retrieval is shown compared to direct radiosonde measurements. Time and date are in UTC time.

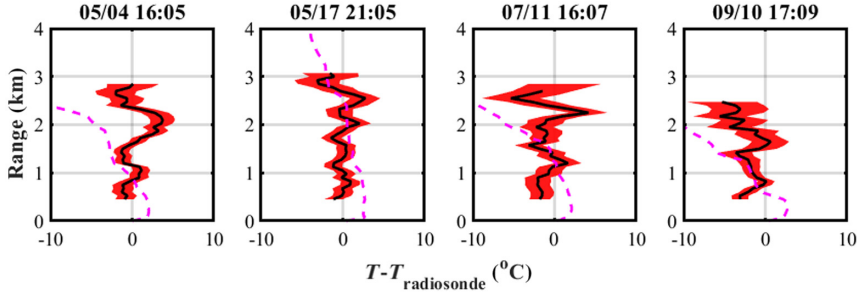

Fig. 5 Temperature difference between DIAL and radiosonde. Error estimates are light red shading. The dry adiabatic lapse rate is shown in the dashed line.

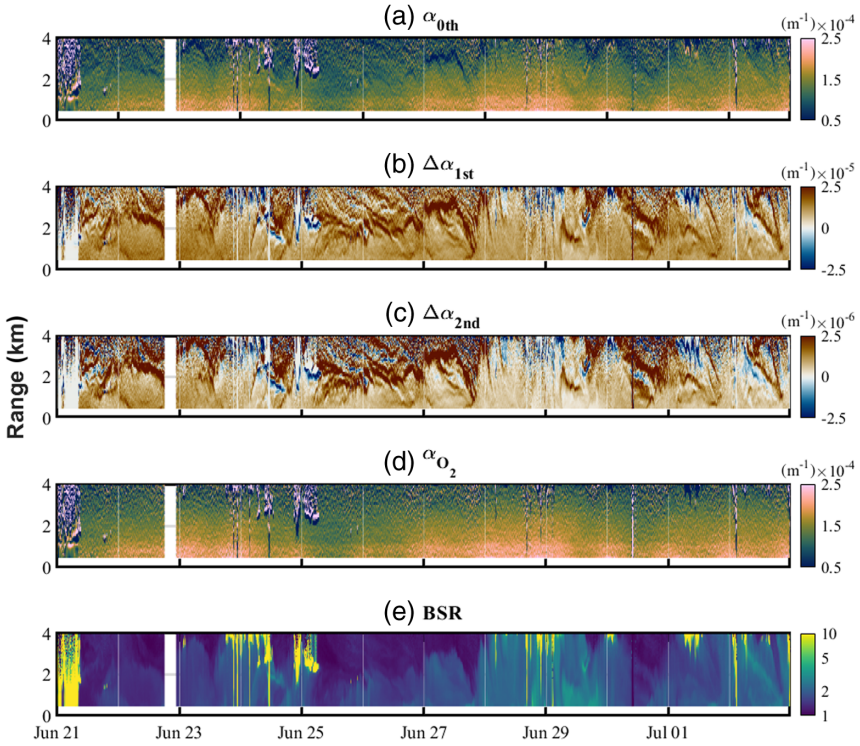

Fig. 6 Section of the MPD data from the same time period as Fig. 3 showing the effect of the BSR on the O_2 absorption and the perturbative correction. (a) The zero-order O_2 absorption coefficient. (b) The first-order correction. (c) The second-order correction. (d) The total observed O_2 absorption coefficient. (e) The BSR. Note the changes in color and scale from (a)–(d). Temporal resolution of data in this figure is 10 min, and range resolution is 75 m. Time ticks are located at 00:00 UTC. The performance of the DIAL and perturbative absorption correction can be seen in aerosol gradients of the BSR.

terms tend to contribute most in two distinct scenarios: (1) when there are strong gradients in the BSR (the DIAL technique depends on the gradient in range and a BSR gradient greatly contributes to Rayleigh–Brillouin error) or (2) when the BSR approaches unity and molecular scattering dominates. (Here, the reduction in absorption due to Rayleigh–Doppler broadening is maximized.)

The efficacy of temperature retrieval was tested using data provided by the radiosondes in two ways. Because the retrieval described is a two-part process (first, perturbative retrieval of the O_2 absorption coefficient and second, iterative conversion of absorption to temperature), it is useful to test each step. To test the former, an O_2 absorption profile calculated from HITRAN parameterizations ($\alpha_{\text{Spectroscopic}}$) using radiosonde temperature, pressure, and WV data was compared to the absorption profile measured using the perturbative retrieval and data from the LiDAR (α_{DIAL}). A plot of the difference between the absorption coefficient profile measured using the LiDAR and the absorption coefficient measured using the data from all 40 radiosondes is shown in Fig. 7. Figure 7(a) shows the absorption difference based on the standard DIAL retrieval, i.e., the zero-order absorption term. As expected, the absorption measured by the LiDAR is about 10% lower than the absorption coefficient calculated using the radiosonde data. This corresponds to a bias of ~ 2.5°C to 6°C and up to 20°C in areas with high aerosol backscatter gradients. Furthermore, large deviations are observed at distinct heights. These correspond to strong aerosol gradients and are the reason Bösenberg[18] concluded that "the incomplete Rayleigh–Doppler correction is the dominant source of error, making this method practically useless for applications in atmospheric research." Figure 7(b) shows the absorption difference as a function of range when the total absorption coefficient is calculated with the perturbative method—the sum of the zero, first, and second-order terms. The absorption difference is now

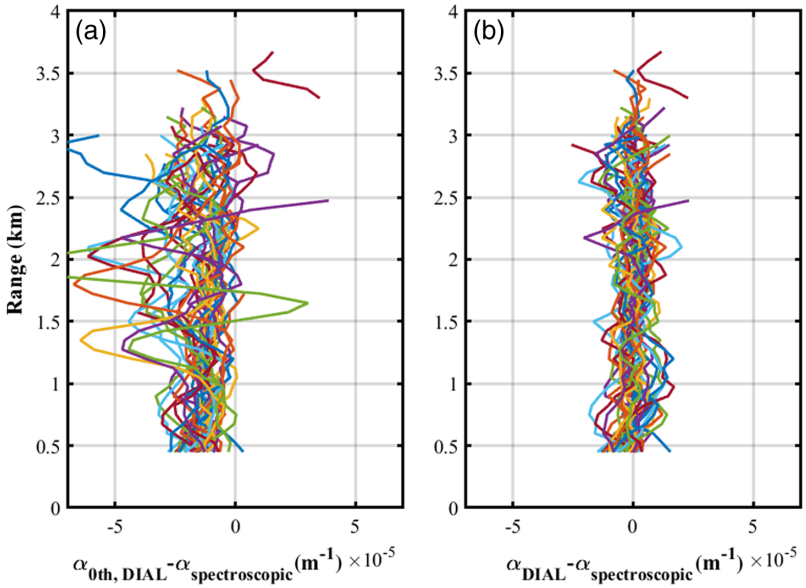

Fig. 7 Comparison of the DIAL O_2 absorption coefficient and modeled O_2 absorption coefficient from radiosonde data shows the performance of the perturbative absorption correction. Each line represents one radiosonde profile. (a) Zero-order O_2 absorption coefficient difference. (b) Total corrected O_2 absorption coefficient difference.

centered near zero with no large spikes, indicating that the perturbative retrieval of the absorption coefficient is correcting for the change in lineshape of the backscattered light.

6.2 Comparison of Iterative Temperature Retrieval with Radiosonde Data

Similar to Sec. 6.1, a test of the second step of the temperature retrieval algorithm was conducted using data from the radiosondes. Note that, although this does not test the accuracy of the spectroscopic model or the perturbative absorption correction (the first step of the DIAL temperature retrieval), it will highlight, in particular, the pressure sensitivity in the spectroscopic model. The calculated absorption profiles from the radiosondes from Fig. 7 ($\alpha_{\text{Spectroscopic}}$) are used as input into the iterative temperature retrieval. The surface temperature, along with a lapse rate of 6.5°C/km, was used as the initial temperature profile (this is only a starting point because the temperature and pressure model will converge to the final temperature profile). Reanalysis data could be used for slightly faster convergence but is not necessary. A pressure profile was then calculated using the surface pressure and the initial guess lapse rate using Eq. (7). The initial temperature profile was updated using Eq. (8) and iterated until convergence (temperature steps $< 0.001^{\circ}$C). Once the iterative temperature retrieval converges, a comparison of the retrieved temperature and pressure profiles with the temperature and pressure profiles measured with the radiosondes ($T_{\text{Spectroscopic}}$ and $P_{\text{Spectroscopic}}$) can be used to assess the efficacy of the iterative temperature retrieval technique. A plot of the temperature and pressure difference between the spectroscopic model and radiosonde measurements as a function of range is shown in Figs. 8(a) and 8(b), respectively.

The maximum temperature difference in Fig. 8 is less than 0.035°C at 5 km, and the maximum pressure difference is less than 0.001 atm up to 5 km. Note that the data range exceeds the observed DIAL observation range as all data originate from sonde measurements. This result indicates that, if one starts with the correct O_2 absorption profile, the iterative temperature retrieval will converge to provide a good estimate of the temperature and pressure profiles (as is suggested by Fig. 7). Using different initial starting temperature lapse rates and pressure using Eq. (7) affects the number of iterations to convergence but does not affect the final value. The addition of the confounding absorption line in the temperature retrieval shown in Sec. 2 removed a bias in the retrieval-sonde comparison by an average of 1.6°C at 400 m and 0.8°C at 4 km using the same comparisons shown in Fig. 8(a). The retrieved temperature is

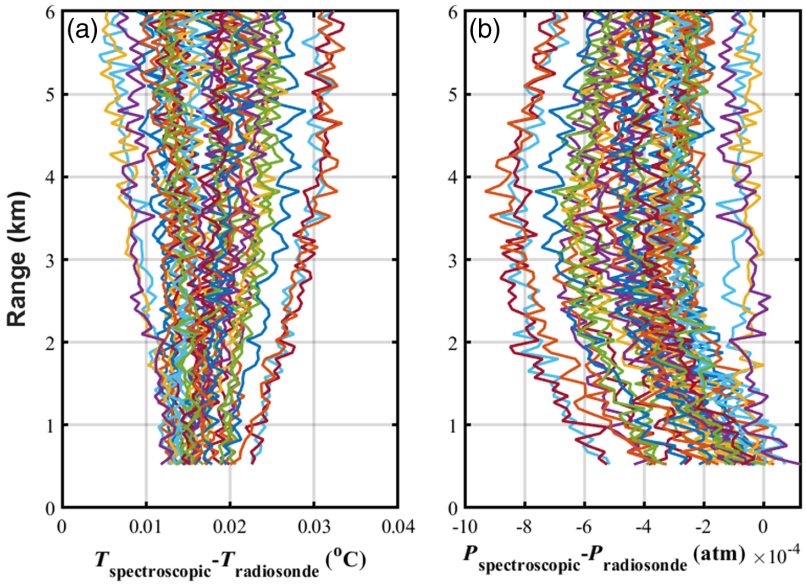

Fig. 8 Similar to Fig. 7 comparing temperature and pressure. (a) Temperature difference (retrieval minus sonde). (b) Pressure difference [Eq. (7) minus sonde]. This figure shows the good performance of the iterative temperature retrieval using collected radiosonde data.

higher without the additional line because a lower calculated absorption in Eq. (8) will result in a higher temperature. The difference changes in height because the absorption lines have different temperature sensitivities and center wavelengths.

6.3 DIAL and Radiosonde Comparisons

A comparison of the radiosonde temperature to the DIAL retrieved temperature is shown in Fig. 9. Using a linear fit to the scatter plot of the temperature retrieved from the LiDAR and the temperature measured using collocated radiosondes shown in Fig. 9(a), a slope of 0.966 and intercept of 0.3144°C were determined with an $R^2 = 0.956$. The fit in Fig. 9(c) has a slope of 0.939 and an intercept of -0.103°C with an $R^2 = 0.945$. In Fig. 9(e), the slope is 0.938 with an intercept of 0.6479°C and an $R^2 = 0.944$. Difference comparisons between radiosonde and LiDAR temperature as a function of altitude show a consistent bias that swings from positive to negative in altitude ~1 km above ground level. This is also seen on time series plots as horizontal banding. Slight horizontal banding can also be observed in WV MPD data in previous work[14,16] as well as in Fig. 3 near 1 km, suggesting the bias stems from something with MPD hardware architecture, perhaps involving the extended overlap function and pulse length. Different instruments and small differences in the alignment of the MPD show different shapes and amplitudes of the bias. In the observational period presented here, the pulse length of the LiDAR transmitter was changed from 1 to 0.75 μs in an attempt to reduce or change the bias. Figures 9(b) and 9(d) show the bias change between a 1 and 0.75 μs pulse length. This effect is currently under investigation.

Each comparison bin has dimensions of 75 m and 10 min. Figures 9(a) and 9(b) have 979 bins for comparison, Figs. 9(c) and 9(d) have 325 bins for comparison. The standard deviation of the temperature difference is 1.95°C (mean -0.315°C) for the 1 μs pulse duration, 1.76°C (mean -0.159°C) for the 750 ns pulse duration, and 2.36°C (mean -0.784°C) for the combined data. The combined data result suggests that the error in the temperature retrieval is approximately $\pm 2.5^{\circ}$C. However, a small bias in range is present, as shown in Fig. 9.

The results of the bootstrapping method of error estimation, theoretically described in Sec. 3, can be seen as the red shaded areas in Figs. 4 and 5. As expected, the error estimate increases with increasing range because the signal-to-noise ratio decreases with increasing range. The error estimate is primarily used as a mask, with the temperature profiles being masked based on a threshold of 5°C in the error estimate. The masks shown in Figs. 2 and 3 show an expected

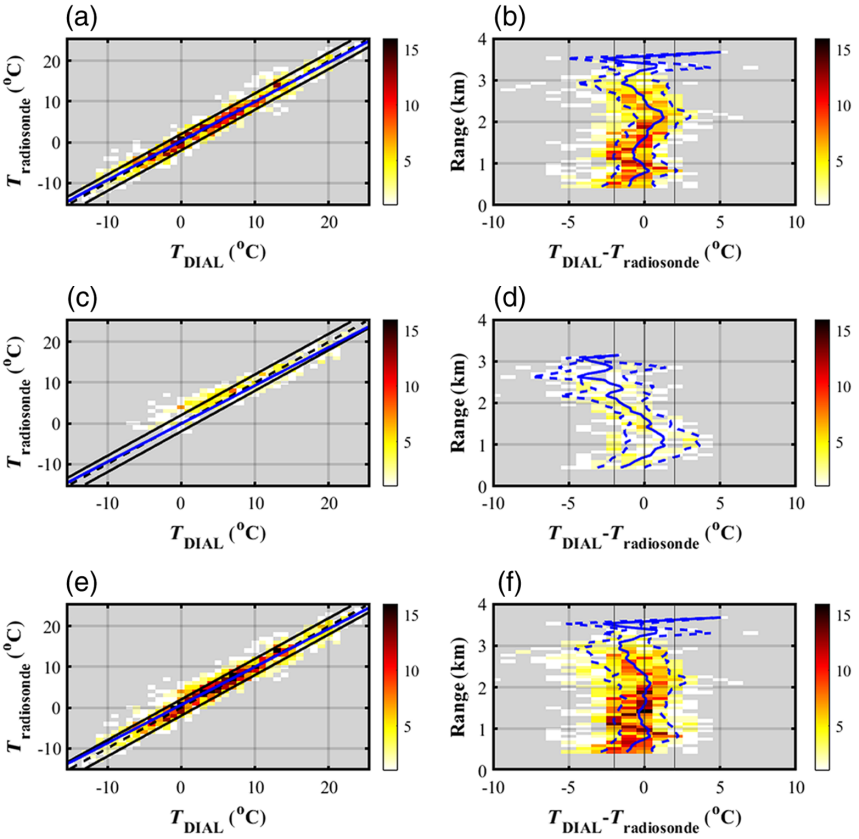

Fig. 9 (a, c, e) Comparisons of radiosondes and DIAL temperature on a 1:1 plot. The blue line is a linear fit. The nlack dashed line is the 1:1 line, and black solid lines are 2°C bounds. (a) Early summer 1 μs pulse length, (c) late summer 0.75 μs, and (e) combined summer comparison. (b, d, f) Comparisons of radiosonde and DIAL temperature difference as a function of range. The blue line is the mean, and dashed blue lines are the standard deviation from the mean. (b) Early summer 1 μs pulse length, (d) late summer 0.75 μs, and (e) combined summer comparison. This figure shows the good performance of the DIAL temperature retrieval compared to radiosonde measurements as well as the consistent bias in altitude.

pattern of masking more during the day because of the higher background noise. The radiosonde comparisons in Fig. 9 show few comparison points beyond $\pm 5^{\circ}$C, meaning the error estimate appears to function well enough to mask data within a threshold.

7 Conclusions

The MPD architecture has been specifically designed to address observational gaps for TD profiling within the lower troposphere. In this study, a laboratory-based instrument—consisting of a subset of the MPD TD-profiling architecture (temperature DIAL without the WV DIAL)—was evaluated to assess the effectiveness of the DIAL temperature retrieval algorithm. This study introduced three key advancements. First, the temperature retrieval was updated by incorporating multiple O_2 absorption lines and using an improved pressure model for the temperature retrieval, thereby enhancing the physical realism. Second, a bootstrapping error estimation method for the temperature retrieval was adapted from a technique originally developed for the WV MPD. Finally, a total of 40 radiosondes were launched from a collocated station with the LiDAR system between April 21, 2022, and September 22, 2022, for evaluation of the accuracy of the DIAL temperature retrieval. These radiosonde data were utilized to evaluate the efficacy of the temperature retrieval in three stages: comparing the perturbative retrieval of absorption against a spectroscopic model using radiosonde data, an assessment of the iterative temperature retrieval

from a spectroscopic model using radiosonde data, and comparing the DIAL temperature retrieval against radiosonde temperature measurements.

Although individual comparisons of the DIAL-based temperature retrieval with radiosondes generally exhibited good agreement (within 2.5°C), some temperature profiles exhibited variation in altitude, albeit without significant bias. Notably, difference comparisons between radiosonde and DIAL-based temperature as a function of altitude consistently revealed a characteristic bias of about 1°C around ∼1 km above ground level. This slight bias may be attributed to a combination of factors, and identifying the exact mechanism and minimizing this bias will be a focus of future work.

This work demonstrates the potential viability of the temperature profiling micropulse DIAL to meet recommendations of resolution and error. Future advances in hardware and signal processing are expected to improve bias and noise error. Temperature profiling combined with WV profiling can provide important retrievals, such as potential temperature and relative humidity for improved performance of numerical weather prediction.

8 Appendix A: All Temperature Comparison Profiles

All radiosonde profiles, along with DIAL temperature profiles and error estimates, are presented in Figs. 10 and 11.

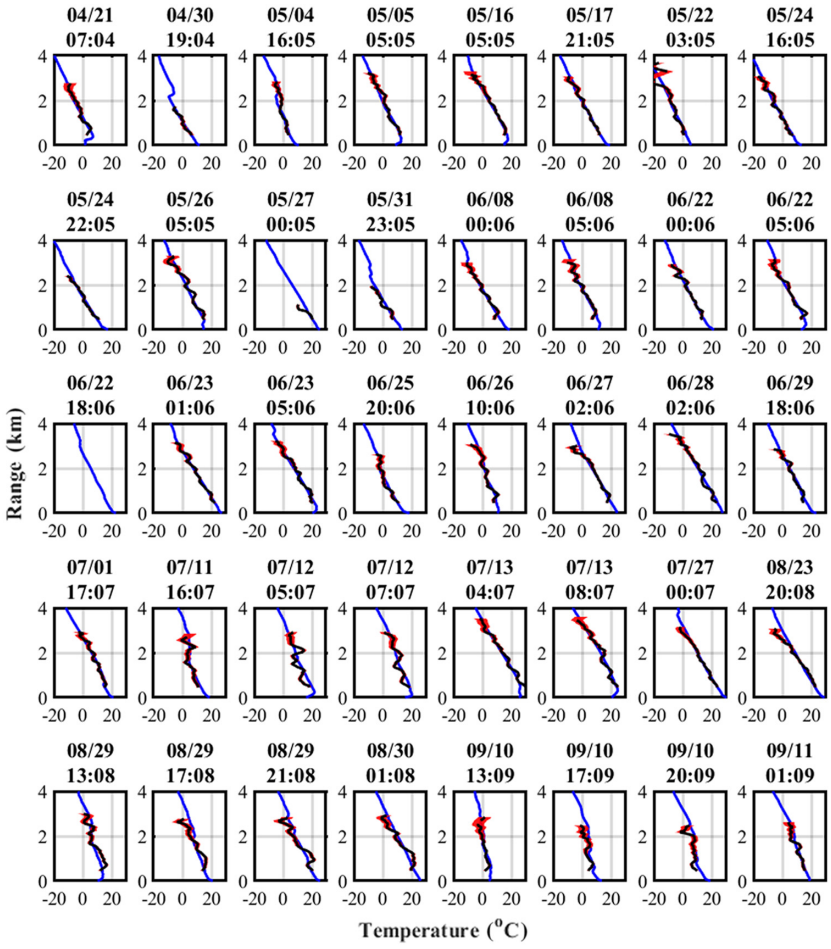

Fig. 10 All radiosonde profiles from the measurement period with the radiosonde temperature in blue, DIAL temperature in black, and error colored in light red shading. Time and date are in UTC time.

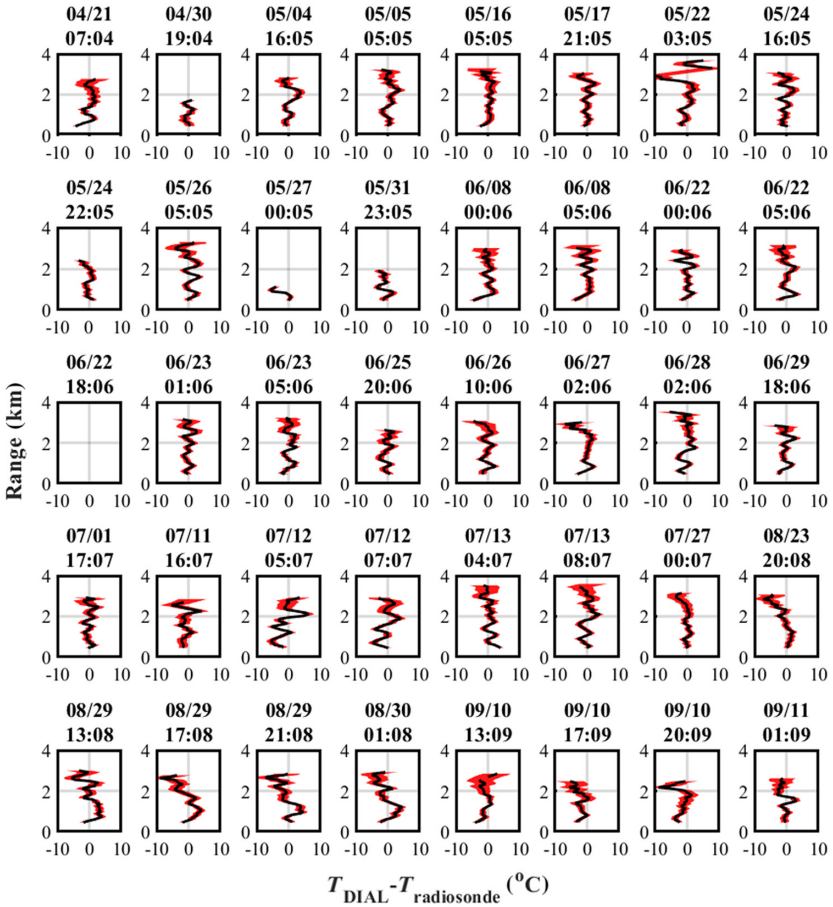

Fig. 11 Temperature difference between DIAL and radiosonde. Error estimates are light red shading. For the 6/22 18:06 profile, the temperature retrieval was masked by the cloud and error mask, so no DIAL data are shown.

Disclosures

The authors declare no conflicts of interest.

Code and Data Availability

Data are available from the authors upon request. Code is available at https://github.com/owen-cruikshank/MicroPuseDIALMSU

Acknowledgments

The National Science Foundation supported this research (Grant No. 1917851). Surface weather station data were provided by the Optical Remote Sensor Lab at Montana State University from Ref. 36.

References

1. National Research Council, *Observing Weather and Climate from the Ground Up: A Nationwide Network of Networks*, National Academies Press, Washington, DC (2009).
2. National Research Council, *When Weather Matters: Science and Services to Meet Critical Societal Needs*, National Academies Press, Washington, DC (2010).
3. R. E. Carbone et al., *Thermodynamic Profiling Technologies Workshop Report to the National Science Foundation and the National Weather Service*, National Center for Atmospheric Research (2012).
4. National Academies of Sciences, Engineering, and Medicine, *The Future of Atmospheric Boundary Layer Observing, Understanding, and Modeling: Proceedings of a Workshop*, p. 25138, National Academies Press, Washington, D.C. (2018).

5. V. Wulfmeyer et al., "A review of the remote sensing of lower tropospheric thermodynamic profiles and its indispensable role for the understanding and the simulation of water and energy cycles," *Rev. Geophys.* **53**(3), 819–895 (2015).
6. H. Lin et al., "Assimilation of New York state mesonet surface and profiler data for the 21 June 2021 convective event," *Mon. Weather Rev.* **151**(2), 485–507 (2023).
7. World Meteorological Organization, "Observing systems capability analysis and review tool," https://space.oscar.wmo.int/observingrequirements (accessed 2024).
8. D. N. Whiteman, "Examination of the traditional Raman LiDAR technique I. Evaluating the temperature-dependent LiDAR equations," *Appl. Opt.* **42**(15), 2571 (2003).
9. D. N. Whiteman, "Examination of the traditional Raman lidar technique II. Evaluating the ratios for water vapor and aerosols," *Appl. Opt.* **42**(15), 2593 (2003).
10. D. Lange, A. Behrendt, and V. Wulfmeyer, "Compact operational tropospheric water vapor and temperature Raman Lidar with turbulence resolution," *Geophys. Res. Lett.* **46**(24), 14844–14853 (2019).
11. R. O. Knuteson, H. E. Revercomb, and F. A. Best, "Atmospheric emitted radiance interferometer. Part I: instrument design," *J. Atmos. Ocean. Technol.* **21**(12), 1763–1776 (2004).
12. R. O. Knuteson, H. E. Revercomb, and F. A. Best, "Atmospheric emitted radiance interferometer. Part II: instrument performance," *J. Atmos. Ocean. Technol.* **21**(12), 1777–1789 (2004).
13. T. Rose et al., "A network suitable microwave radiometer for operational monitoring of the cloudy atmosphere," *Atmos. Res.* **75**(3), 183–200 (2005).
14. R. A. Stillwell et al., "Demonstration of a combined differential absorption and high spectral resolution LiDAR for profiling atmospheric temperature," *Opt. Express* **28**(1), 71–93 (2020).
15. S. M. Spuler et al., "MicroPulse DIAL (MPD) - a diode-laser-based lidar architecture for quantitative atmospheric profiling," *Atmos. Meas. Tech.* **14**(6), 4593–4616 (2021).
16. T. M. Weckwerth et al., "Validation of a water vapor micropulse differential absorption lidar (DIAL)," *J. Atmos. Ocean. Technol.* **33**(11), 2353–2372 (2016).
17. F. A. Theopold and J. Bösenberg, "Differential absorption lidar measurements of atmospheric temperature profiles: theory and experiment," *J. Atmos. Ocean. Technol.* **10**(2), 165–179 (1993).
18. J. Bösenberg, "Ground-based differential absorption lidar for water-vapor and temperature profiling: methodology," *Appl. Opt.* **37**(18), 3845–3860 (1998).
19. K. S. Repasky et al., "Modeling the performance of a diode laser-based (DLB) micro-pulse differential absorption lidar (MPD) for temperature profiling in the lower troposphere," *Opt. Express* **27**(23), 33543–33563 (2019).
20. C. E. Bunn et al., "Perturbative solution to the two-component atmosphere DIAL equation for improving the accuracy of the retrieved absorption coefficient," *Appl. Opt.* **57**(16), 4440–4450 (2018).
21. J. B. Mason, "Lidar measurement of temperature: a new approach," *Appl. Opt.* **14**(1), 76–78 (1975).
22. I. J. Barton and J. F. Marshall, "Differential-absorption lidar measurements in the oxygen a band using a ruby lidar and stimulated Raman scattering," *Opt. Lett.* **4**(3), 78–80 (1979).
23. C. L. Korb and Chi. Y. Weng, "Differential absorption lidar technique for measurement of the atmospheric pressure profile," *Appl. Opt.* **22**(23), 3759–3770 (1983).
24. A. Ansmann, "Errors in ground-based water-vapor DIAL measurements due to Doppler-broadened Rayleigh backscattering," *Appl. Opt.* **24**(21), 3476–3480 (1985).
25. C. D. Boley, R. C. Desai, and G. Tenti, "Kinetic models and Brillouin scattering in a molecular gas," *Can. J. Phys.* **50**(18), 2158–2173 (1972).
26. G. Tenti, C. D. Boley, and R. C. Desai, "On the kinetic model description of Rayleigh–Brillouin scattering from molecular gases," *Can. J. Phys.* **52**(4), 285–290 (1974).
27. I. Binietoglou, P. Giampouras, and L. Belegante, "Linear approximation of Rayleigh–Brillouin scattering spectra," *Appl. Opt.* **55**(27), 7707–7711 (2016).
28. I. E. Gordon et al., "The HITRAN2016 molecular spectroscopic database," *J. Quant. Spectrosc. Radiat. Transf.* **203**, 3–69 (2017).
29. B. J. Drouin et al., "Multispectrum analysis of the oxygen A-band," *J. Quant. Spectrosc. Radiat. Transf.* **186**, 118–138 (2017).
30. V. D. Galkin, "Electronic moment of the b1Σg+ - X3Σg− transition of the oxygen band system," *Opt. Spectrosc.* **47**(2), 151–153 (1979).
31. E.V. Browel, S. Ismail, and B. E. Grossman, "Temperature sensitivity of differential absorption lidar measurements of water vapor in the 720-nm region," *Appl. Opt.* **30**(12), 1517–1524 (1991).
32. M. Hayman and S. Spuler, "Demonstration of a diode-laser-based high spectral resolution lidar (HSRL) for quantitative profiling of clouds and aerosols," *Opt. Express* **25**(24), A1096–A1110 (2017).
33. M. Hayman, R. A. Stillwell, and S. M. Spuler, "Fast computation of absorption spectra for lidar data processing using principal component analysis," *Opt. Lett.* **44**(8), 1900–1903 (2019).
34. M. Hayman, R. A. Stillwell, and S. M. Spuler, "Optimization of linear signal processing in photon counting lidar using Poisson thinning," *Opt. Lett.* **45**(18), 5213–5216 (2020).

35. M. Hayman et al., "Global estimation of range resolved thermodynamic profiles from micropulse differential absorption lidar," *Opt. Express* **32**(8), 14442–14460 (2024).
36. J. Shaw, "OSRL weather station," https://www.montana.edu/orsl/weather.html (accessed 2022).

Owen Cruikshank is a graduate student in the Electrical and Computer Engineering Department at Montana State University pursuing a PhD in electrical engineering. He received his BS degree in physics from Michigan Technological University in 2018 and his MS degree in optics and photonics from Montana State University in 2021. His research area is optical remote sensing.

Luke Colberg is a graduate student in the Electrical and Computer Engineering Department at Montana State University currently pursuing a PhD in electrical engineering. He received his BS degree in mechanical engineering and his MS degree in optics and photonics from Montana State University in 2019 and 2021, respectively. His research area is optical remote sensing.

Kevin S. Repasky received his BSEng degree in mechanical engineering from Youngstown State University in 1988 and his MS degree and PhD in physics from Montana State University in 1992 and 1996, respectively. Currently, he is a professor in the Electrical and Computer Engineering Department at Montana State University. His research interests include laser design and development, nonlinear optics, optical remote sensing, and optical communications.

Robert A. Stillwell is a software engineer at the National Center for Atmospheric Research. He received his BS and MS degrees and his PhD from the University of Colorado at Boulder in aerospace engineering in 2013, 2013, and 2017, respectively. His research interests include optical system design and remote sensing of the atmosphere.

Scott M. Spuler is a research engineer at the National Center for Atmospheric Research. He received his MS degree and PhD in applied optics/engineering systems from Colorado School of Mines in 1999 and 2001, respectively. His research interests include the development of innovative optical and laser-based instrument systems that can be applied to enhance the understanding of the atmosphere.